Precision Engineering 99 (2026) 632–642

Contents lists available at ScienceDirect

Precision Engineering

journal homepage: www.elsevier.com/locate/precision

A dual-joint compliant architecture for precision control in robotic neuroendoscopy

Federico Mariano [a,b,*], Elena De Momi [b], Giovanni Berselli [a,c], Jovana Jovanova [d], Leonardo S. Mattos [a]

[a] Biomedical Robotics Lab, Department of Advanced Robotics, Istituto Italiano di Tecnologia, Genoa, Italy
[b] Department of Electronics, Information and Bioengineering, Politecnico di Milano, Milan, Italy
[c] DIME, Università di Genova, Genoa, Italy
[d] Department of Maritime and Transport Technology, Delft University of Technology, Delft, The Netherlands

ARTICLE INFO

Keywords:
Compliant joint
Remote Center of Motion
Finite element methods
Minimally invasive surgery

ABSTRACT

Neuroendoscopy treats intracranial pathologies through millimeter-scale channels using endoscopes introduced along a straight trajectory from a cranial entry point to the target. The entry point acts as a Remote Center of Motion (RCM), which must remain fixed to follow the surgical plan and avoid damage around the entry point. Existing robotic RCM platforms rely on rigid multi-link structures, increasing complexity and footprint. To mitigate these limitations, we propose a compact dual-joint compliant mechanism for neuroendoscopic manipulation. Building on the Tetra II flexure architecture, we redesigned and optimized the joint for neurosurgical use. The end-effector holder is moved from the central axis to the side to improve visual access, facilitate sterile draping and allow rapid instrument exchange while preserving the RCM constraint. The mechanical design targets directionally uniform stiffness in the working plane while minimizing parasitic RCM displacements. The mechanism uses two identical compliant joints in series, with the connection angle treated as a design variable. For each angle, the response is obtained by analyzing each joint separately in FEM and combining their contributions via rotation matrices. An angular offset of 300° yields near-isotropic stiffness, with a root-mean-square error of 0.90 N/m from an ideal isotropic behavior. A PA12 prototype was tested under 0.1 ± 0.01 N radial loads. Experimental stiffness differed by ≤19% from FEM. The parasitic RCM displacement was 0.032 ± 0.018 mm for a 4.5° shaft rotation, well within the 1 mm neurosurgical tolerance. This dual-joint compliant RCM mechanism offers a practical alternative to conventional rigid-link designs.

1. Introduction

As a minimally invasive surgical technique (MIS), neuroendoscopy employs a neuroendoscope to treat various brain disorders [1]. The procedure begins with a small scalp incision, followed by the creation of a cranial burr hole, a precisely drilled opening in the skull that serves as an entry pathway for endoscope insertion. By accessing deep anatomical structures and providing clear visualization of otherwise hidden brain regions [2,3], the neuroendoscope enables precise interventions with minimal damage to surrounding tissues. A key factor in reducing tissue damage is adhesion to the Remote Center of Motion (RCM) principle, where a fixed pivot point in space remains unchanged during endoscope motions [4,5]. By positioning this RCM in the burr hole, surgeons can orient the endoscope to accurately follow a preplanned insertion trajectory towards the target anatomy starting at the burr hole.

Commercial systems that embody the concept of RCM include the ROSA One Brain, a stereotactic platform with an articulated arm of six degrees of freedom that achieves submillimetric targeting accuracy while allowing frameless and minimally invasive access to deep cerebral structures [6]. In addition, the NeuroMate robot, the first FDA-approved neurosurgical robot, has shown a mean phantom targeting error of 1.29 mm [7]. Beyond these market-ready solutions, the literature describes double parallelogram linkages, built from two four-bar parallelograms that keep all rotations about a fixed pivot [8]; spherical mechanisms, in which several revolute joints intersect at a common point that serves as the RCM [9]; virtual RCMs, created in software by constraining a generic robot through real-time kinematic control [10]; and finally compliant joint solutions that, although still rarely used in the surgical field, have potential for generating innovative solutions [11].

* Corresponding author at: Biomedical Robotics Lab, Department of Advanced Robotics, Istituto Italiano di Tecnologia, Genoa, Italy.
E-mail address: federico.mariano@iit.it (F. Mariano).

https://doi.org/10.1016/j.precisioneng.2026.02.012
Received 30 July 2025; Received in revised form 9 January 2026; Accepted 14 February 2026
Available online 18 February 2026

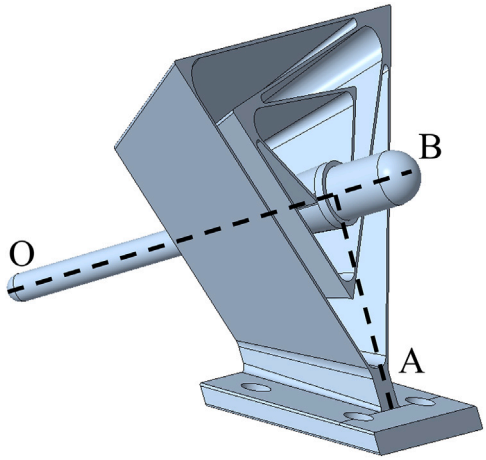

Fig. 1. Compliant joint Tetra II [14]. Point *A* is the fixed base attachment, point *B* is the distal interface where an external driving force is applied, causing rotations around point *O*. The dashed line *OB* indicates the moving shaft of the joint corresponding to the end-effector.

Unlike conventional rigid link designs, compliant joints can achieve motion through elastic deformation of their material, eliminating the need for multiple mechanical components [12]. When the entire mechanism is produced as a single piece, it is referred to as a monolithic compliant mechanism [13]. An example of this type of joint is the Tetra II joint, shown in Fig. 1, proposed by Rommers et al. [14]. Inspired by the "infinity hinge" [15,16], it is composed of three interconnected tetrahedrons which are carefully arranged in a nested configuration, enabling pure rotational motion around the RCM without unwanted translation. In this design, all structural walls must be oriented toward the RCM to preserve this behavior. In particular, as long as the essential flexure mechanics remain intact, variations in the internal geometry of each tetrahedron do not affect the fundamental operation of the joint.

Although the Tetra II joint satisfies the essential kinematic requirements of RCM, several limitations prevent its direct use in the intended surgical application. To address the shortcomings, we present a new compliant RCM mechanism based on Tetra II concepts. The new design aims to address the constraints and requirements of neurosurgical procedures, such as Endoscopic Third Ventriculostomy (ETV) to treat hydrocephalus. The expected benefits include reduced footprint, friction, wear, backlash, and overall complexity while maintaining the precision typically associated with rigid body mechanisms [17].

Overall, the contributions of this work include: (i) A dual-compliant, off-axis monolithic RCM joint for robotic neuroendoscopy that improves intraoperative visibility, simplifies sterile draping and rapid endoscope exchange, supports tissue-sparing manipulation in ETV and related neuroendoscopic procedures while having near isotropic stiffness behavior and drastically reducing the parasitic error obtained at the RCM point; (ii) an hybrid analytical/Finite Element Methods (FEM) based modeling methodology decomposes the dual-compliant joint into its upper (J1) and lower (J2) stages, solves them independently and maps their displacement fields into a common reference frame through rotation matrix transformations to predict end-effector motion and directional stiffness without the need to create CAD models. This approach delivers excellent results without the need to generate multiple CAD geometries, which saves significant time.

The remainder of this manuscript is organized as follows. Section 2 synthesizes the functional, mechanical, and clinical requirements the joint must satisfy to allow deployment in the operating theater. Section 3 details the structural design proposed to enable the use of the mechanism for the intended neurosurgical application, investigating its behavior and performance through FEM analysis and experimental validation. Particular attention was placed on analyzing the stiffness anisotropy of the mechanism, the parasitic displacements of its RCM point and the stiffness behavior along non-working direction. Section 4 presents the experimental data, which allows identifying a design that produces an optimal stiffness behavior with minimal parasitic RCM displacement. Finally, Section 5 contextualizes these findings and outlines their implications considering future clinical use.

2. Design requirements

The proposed compliant joint was designed to allow precise positioning of the endoscope within the patient's cranial cavity. The following requirements define the key functional and performance specifications of the system.

- **Sterility management:** The joint must be designed to ensure a clear separation between sterile components and those that cannot undergo sterilization. Therefore, it shall accommodate a sterile drape to isolate non-sterilizable components.
- **Unobstructed surgical field:** The joint must be designed to avoid occlusion of the surgeon's line of sight, particularly around the endoscope entry point, to maintain optimal visualization of the surgical field.
- **Quick-release mechanism:** The end effector must be easily and intuitively removable to allow rapid instrument exchange or emergency unlock in case of malfunction.
- **Material requirement:** The device must be made of biocompatible material. Components that cannot be draped must be of a material that supports autoclave processing or another appropriate sterilization process.
- **Isotropic stiffness:** The mechanism shall exhibit isotropic stiffness behavior for the orientation of the surgical instrument in relation to the RCM, which means uniform resistance to pitch and roll deflections. This characteristic facilitates the future implementation of a motorized closed-loop control strategy. In fact, a highly non-isotropic system could hinder or block the rotation of the joint along certain directions, preventing optimal operation and compromising the overall performance of the mechanism.
- **Workspace:** The intended application of the proposed joint mechanism is neuroendoscopy for operations within the third ventricle. Therefore, based on average anatomical dimensions such as the width of the ventricle and the distance from the burr hole to the ventricular floor [18], the minimal angular excursion needed to access the lateral walls of the third ventricle can be estimated to be approximately 4.5°. Furthermore, to allow a precise orientation of the instrument about the RCM before insertion, we estimate that ±15° from an initial rough manual orientation should be sufficient. Consequently, the required roll and pitch deflections are given by the larger of these two constraints, i.e., the joint should provide at least ±15°.
- **Parasitic error constraint:** The parasitic displacement of the RCM point must remain within a 1 mm threshold to avoid unnecessary damage to brain tissue. This error level is comparable to those of existing neuroendoscopic guidance systems [19].
- **Safety in non-working direction:** While low stiffness is required in the working plane to allow controlled pivoting around the RCM, the joint must remain sufficiently stiff in non-working directions to avoid unintended motion of the endoscope. In particular, perturbations along the shaft axis and lateral components that are not aligned with the commanded rotation should not produce large off-axis deflections of the instrument. To this end, the mechanism must be designed to exhibit a much higher stiffness along the shaft direction rather than in the working direction.

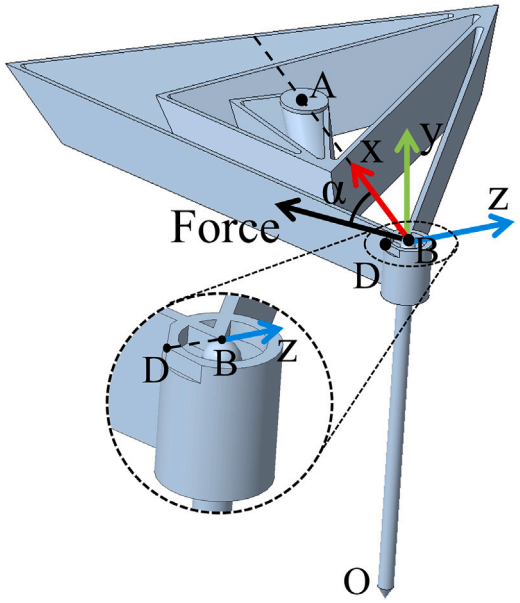

Fig. 2. Redesigned compliant joint with remote center of motion: Point A is the joint's fixation point, while point B is where the external driving force is applied, pivoting the shaft OB about the point O. The shaft OB represents the device to be oriented (e.g., a neuroendoscope). Point D is an auxiliary point defined on a flat surface of the link to facilitate its localization in the FEM model. Point B and D are rigidly connected but used as distinct markers to reconstruct the local orientation of the joint.

3. Design of the new compliant joint for neuroendoscopy

The new design aims to satisfy the application requirements listed above. The first points are addressed by positioning the surgical instrument holder outside the tetrahedral structure, as shown in Fig. 2. In addition, the fixation point (point A in Fig. 2) is placed in the central position. This arrangement offers three immediate advantages: (i) creates a distinct separation between the joint and the end effector, allowing the application of a sterile drape; (ii) relocates the mechanism away from the visualization axis, thus preserving the surgeon's view of the cranial entry point; (iii) facilitates the implementation of a quick disconnect mechanism that would not require moving the neuroendoscope to remove the positioning mechanism from the surgical environment in case of failure or emergency.

The design illustrated in Fig. 2 was evaluated in both simulations and using a physical prototype fabricated by Selective Laser Sintering (SLS). However, the results demonstrated high non-isotropic stiffness and relatively large parasitic errors, as shown in Figs. 9a and 10. Therefore, here we propose the use of a second compliant element added in series with the first one to enhance the joint's mechanical performance. Specifically, the instrument of Joint 1 (J1) is connected to the fixation point of Joint 2 (J2), as illustrated in Fig. 3a.

To provide further intuition, each compliant joint can be interpreted as two springs connected in series. When two such joints are connected in series their equivalent stiffness, K_{tot}, along a given direction is governed by relation shown in Eq. (1)

$$\frac{1}{K_{tot}} = \frac{1}{K_1} + \frac{1}{K_2}, \tag{1}$$

where K_1 and K_2 denotes the stiffness of the two springs. If one of the two stiffness values tends to infinite, the total stiffness tends to the value of the other.

Translating this concept to our dual-joint architecture, each compliant joint can be seen as a direction-dependent spring. When two such joints are connected in series and their stiffness patterns are angularly shifted, directions in which one joint is very stiff are combined with directions in which the other joint is relatively compliant. In those directions, the equivalent stiffness is dominated by the more compliant joint. Extending this reasoning over all loading directions, the combination effectively reduces the peaks of stiffness and results in a quasi-isotropic overall stiffness for the dual-joint system.

The intricate geometry of the proposed structure does not allow for an easy analytical calculation of its stiffness in different directions. To overcome this limitation, we adopted a hybrid analytical/FEM workflow. First, the displacements of J1 and J2 were obtained separately with ANSYS. Because the connection angle (γ in Fig. 3b) between the two joints was swept from 0° to 360° in 15° increments, obtaining 24 configurations, each displacement was rotated into a common reference frame using the appropriate rotation matrices and then superimposed. The combined displacements provide the end effector rotation from which the stiffness is extracted. This approach allows us to analyze all 24 configurations without generating a new CAD model for each case, thereby reducing pre-processing time. This overall hybrid analytical/FEM workflow used to obtain the end-effector translation and stiffness is summarized in Fig. 4.

3.1. Modeling of the serial flexure for hybrid analytical/FEM based analysis

The same tetrahedral geometry was used in both flexures, as shown in Fig. 3a. The two joints are connected by linking the instrument of the first joint to the fixation point of the second joint. The connection angle, indicated as γ and illustrated in Fig. 3b, is a key variable in our study.

This model simplified the two joints with two beams of lengths l_1 and l_2. The second beam was connected to the first at point B at an angle γ relative to the y-axis. The length l_1 corresponds to the radius of the circle visible in Fig. 3a, and is defined as 75 mm. The length l_2 depends on the height of the end effector from the RCM, visible in Fig. 3c. J1 is located at 100 mm from the RCM, while J2 is at 75 mm from the RCM. The angle β is therefore obtained as follows:

$$\beta = \arctan\left(\frac{h_2}{r_2}\right) = \arctan\left(\frac{h_1}{l_2}\right), \tag{2}$$

where h_2 is the height of J2, r_2 is the radius of the circle that circumscribes the triangle shown in Fig. 3a, and h_1 is the height of J1. Since both joints share the same geometry, we can conclude that $r_1 = r_2 = 75$ mm. Using Eq. (2), we obtain the length value l_2 equal to 100 mm. The design of the wall thickness t and joint height H_j was constrained by both structural integrity and manufacturability. Because the flexural thickness decreases along the direction towards the RCM, upper and lower bounds on t had to be defined in combination with a suitable value of H_j. Thicknesses below 1 mm were found to be too weak and prone to damage, whereas excessively large values of H_j would require an undesirable reduction in wall thickness, compromising the compliance of the joint. On this basis, the final design adopts a maximum flexure thickness of 1.4 mm, resulting in a minimum thickness of 1.12 mm and a joint height $H_j = 15$ mm.

These dimensions were selected in view of the capabilities of the ProX 6100 system and the chosen additive manufacturing process, Selective Laser Sintering (SLS). Among the available additive techniques, SLS because it provides the most reliable reproduction of the thin flexure features required in this application, while ensuring final prototypes with a low incidence of manufacturing defects.

Optimization of the proposed mechanism to ensure isotropic stiffness was performed by varying the angle γ from 0° to 360° in increments of 15°. Then each configuration was analyzed by applying a force F to the point C in different α angles in the x-z plane. The stiffness was obtained using the following equation.

$$k = F/x, \tag{3}$$

where F corresponds to the force used in the simulation and x is the displacement obtained at the point C.

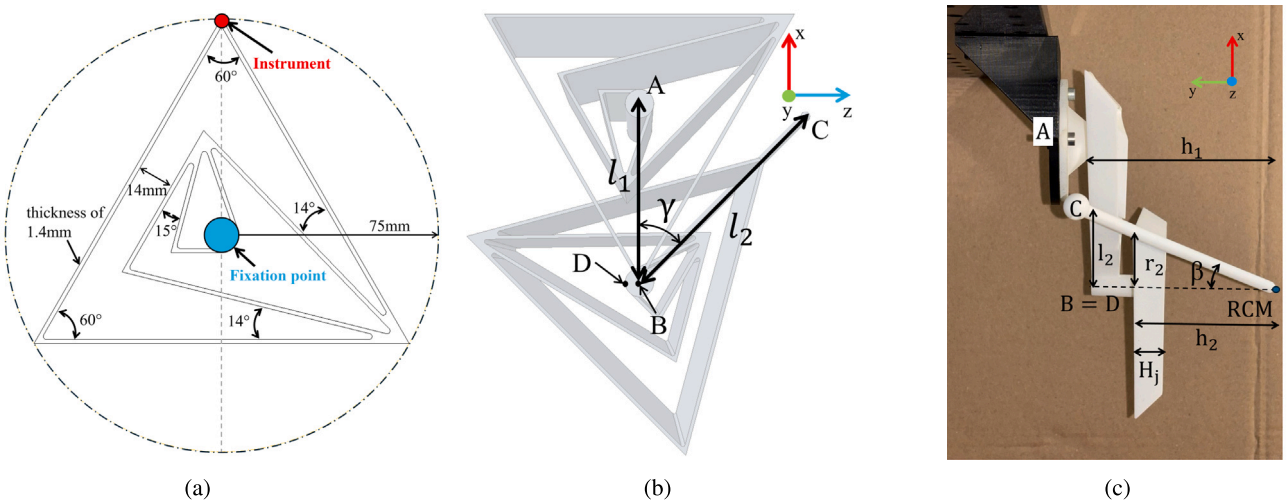

(a) (b) (c)

Fig. 3. (a) Geometry of the tetrahedrons used for each joint. - (b) Upper view of a configuration of two joints in series. - (c) Lateral view of the same dual-joint configuration. In the proposed implementation, $h_1 = 100$ mm and $h_2 = 75$ mm.

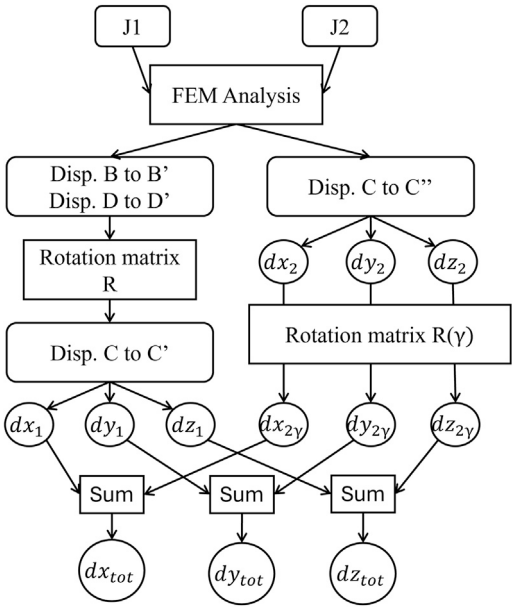

Fig. 4. Workflow used to obtain the end-effector translation from the dual-compliant joint.

The simulation was divided into two parts, simulating J1 and J2 separately. After running both simulations, their displacements are transformed using rotational matrices to align each coordinate system, and the total displacement of the point C is obtained by summing the individual contributions. The reference points used for the two simulations, explained in the following section, are summarized in Table 1.

3.2. FEM evaluation of the dual-joint system with variable offset

The simulation for J1 must account for translational and rotational effects. Specifically, the displacement of point B, resulting from the force applied on the point C, is calculated simulating a force F, at the point B while varying the direction of the applied force α. In addition, the simulation also accounts the moment M generated by the force F and its lever arm which depends by the direction of the force α and the connection angle between the joints γ obtaining as value of M:

$$M = L_{BC} F sin(\alpha - \gamma), \tag{4}$$

where L_{BC} is the distance from point B to point C.

These two contributions are evaluated independently using FEM analysis in ANSYS by constraining point A and applying the force F and moment M at point B, from which the displacements of points B and D are obtained. In the CAD and FEM models, a small flat area, shown in Fig. 2, is added at point D purely to allow unambiguous node selection in Ansys. Point D is rigidly connected to B and serves as an auxiliary marker: the vectors $\overrightarrow{OB}$ and $\overrightarrow{BD}$ define the local reference frame and allow us to reconstruct its 3D orientation from the FEM displacement.

All FEM simulations were performed using tetrahedral elements, each composed of 4 nodes. To ensure numerical precision and independence of the mesh, a convergence criterion was set: the mesh was iteratively refined until the relative change in displacement values between two successive refinements was less than 1%. This procedure guaranties that the displacement field is sufficiently resolved and that the simulation outputs are not sensitive to the granularity of the mesh. The entire joint was modeled as a deformable PA12 body with density of $\rho = 1,01e-06$ kg/mm^3, Young Modulus of $E = 1207$ MPa, Poisson ratio of $\nu = 0.414$. The distinction between compliant and quasi-rigid regions is achieved through geometry and boundary conditions. The thin panels of the flexure links provide the compliance and carry almost all of the elastic deformation, whereas the thicker connection blocks between the flexures (including the fixed base around point A, the connection region at B, and the end-effector interface) are fully constrained or kinematically coupled so that they behave effectively as rigid links within the investigated load range.

Once the displacements of J1 and J2 are known, the total displacement of the point C is obtained by summing the contributions expressed in a common reference frame. Initially, since the points B and C are rigidly connected and the deformation due to the second joint is not yet applied, the intermediate displacement of the point C is calculated by rotation of the frame associated with point B.

As shown in Fig. 5, a local reference system (x, y, z) is defined in B. The unit vector y is aligned with the shaft and obtained from the vector connecting O to B, while unit vector z is obtained from the vector connecting B to the auxiliary point D. The unit vector x is then defined by the right-hand cross product of y and z ensuring an orthonormal frame at B. The relevant expressions are given in Eqs. (5)–(7), and the coordinates of the points O, B, D and C are reported in Table 2.

$$y = \frac{B - O}{\|B - O\|} \tag{5}$$

Table 1
Description of reference points and variables used in the geometric model and FEM simulations.

	Description	
γ	Angular offset between the two compliant joints in the dual-joint configuration, which determines their combined mechanical behavior and influences the isotropy of the overall stiffness	Variable
α	Is the angle of the applied external force with respect to the reference frame of the joint, used to evaluate the directional stiffness response in FEM simulations	
A	Fixation point, assumed as the fixed base point of the dual-joint structure in the FEM simulations. It remains static and serves as the anchoring reference for applied forces and deformations.	Initial configuration
O	RCM point used as the global reference for rotations.	
B	End of Joint 1 and base of Joint 2. Connection point between the two compliant joints.	
C	Attachment point of the instrument shaft. Target of displacement measurements obtained during the simulations and physical experiments.	
D	Auxiliary point rigidly connected to B for defining the local coordinate system.	
B'	Deformed position of B after Joint 1 simulation. Used for computing rotation.	Simulation 1
C'	Intermediate position of point C after deformation from Joint 1 only. Used, along with C'', to compute the total displacement of the end-effector.	
D'	Deformed position of D after Joint 1 simulation. Used to update local orientation.	
C''	Final position of point C after deformation from both joints. Combined with C' to determine the total end-effector displacement.	Simulation 2

Table 2
Coordinates of the key points in the reference system.

Coordinates			
Point	x	y	z
O	−75 mm	0 mm	0 mm
B	−75 mm	100 mm	0 mm
D	−75 mm	100 mm	−6 mm
C	$l_2\cos(\gamma)$	100 mm	$l_2\sin(\gamma)$

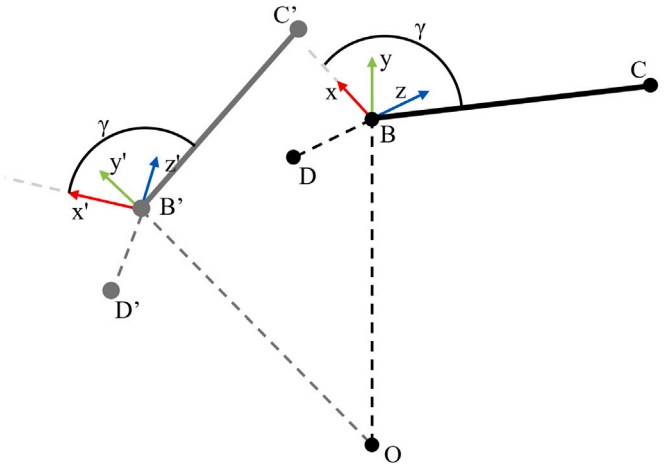

Fig. 5. Representation of the movement of point B and C in reaching points B' and C'.

$$z = \frac{B - D}{\|B - D\|} \tag{6}$$

$$x = y \times z \tag{7}$$

After applying the force, the point B moves to B', while the points D and C move to D' and C', respectively. The axes (x', y', z') in B' are defined again using the Eqs. (5)–(7) by substituting B with B' and D with D'.

To determine the coordinates of C', the rotation matrix is constructed using the computed unit vectors x', y', z' as its rows.

$$R = \begin{bmatrix} x' \\ y' \\ z' \end{bmatrix}. \tag{8}$$

Finally, the coordinates of C' are found by:

$$C' = O + R(C - O). \tag{9}$$

This formulation ensures an accurate evaluation of the deformations affecting the end effector due to the displacement of the joint.

The displacement of J2 was determined using a more straightforward approach. In this case, the simulation was performed by fixing the point B and applying the force at the point C, oriented along the direction defined by the angle α in the $x - z$ plane, moving the point C to C''. This applied force had the same magnitude as the one used in the simulation of J1. The output of this simulation provided the coordinates of point C'', which were then used to determine the displacement of point C obtained during the entire transformation.

To compute the total displacement of the joint system, the displacement values of J1 and J2 were summed. Since the reference frames between the two joints rotate by an angle γ, a second rotation matrix $R(\gamma)$ was used to derive the total displacement values. The final displacement components are given by:

$$\begin{aligned} dx_{tot} &= dx_1 + dx_{2\gamma}, \\ dy_{tot} &= dy_1 + dy_{2\gamma}, \\ dz_{tot} &= dz_1 + dz_{2\gamma}, \end{aligned} \tag{10}$$

where dx_{tot}, dy_{tot}, and dz_{tot} represent the total displacement of point C obtained on the joint in series. The terms dx_1, dy_1, and dz_1 correspond to the displacement obtained for the point C' during the simulation of J1, whereas $dx_{2\gamma}$, $dy_{2\gamma}$, and $dz_{2\gamma}$ represent the displacement of the point C'' during the simulation of J2, which was previously rotated by the angle γ. The displacement components for the rotated joint are given by:

$$\begin{bmatrix} \mathrm{d}x_{2\gamma} \\ \mathrm{d}y_{2\gamma} \\ \mathrm{d}z_{2\gamma} \end{bmatrix} = R(\gamma) \begin{bmatrix} \mathrm{d}x_2 \\ \mathrm{d}y_2 \\ \mathrm{d}z_2 \end{bmatrix} \tag{11}$$

corresponding to:

$$\begin{bmatrix} \mathrm{d}x_{2\gamma} \\ \mathrm{d}y_{2\gamma} \\ \mathrm{d}z_{2\gamma} \end{bmatrix} = \begin{bmatrix} \cos\gamma & 0 & -\sin\gamma \\ 0 & 1 & 0 \\ \sin\gamma & 0 & \cos\gamma \end{bmatrix} \begin{bmatrix} \mathrm{d}x_2 \\ \mathrm{d}y_2 \\ \mathrm{d}z_2 \end{bmatrix}, \tag{12}$$

where $R(\delta)$ is the rotation matrix corresponding to a rotation of angle γ about the global y-axis, dx_2, dy_2, and dz_2 are the displacement values of point C'' obtained from the simulation of J2.

3.3. Validation of the analytical stiffness model through FEM comparison

This section aims to validate the hybrid analytical/FEM procedure described in Section 3.1 by comparing its results with the FEM-based analysis of detailed 3D CAD models of the complete dual-joint compliant mechanism.

Four flexure samples, corresponding to connection angles (γ) of 180°, 225°, 270°, and 315°, were analyzed to validate the analytical approach. For each configuration, a CAD model was generated using Creo Parametric to capture the specific geometry of the flexures. FEM simulations were then performed in ANSYS to compute the stiffness values, which were compared to the predictions presented in the previous section. The observed differences were quantified by calculating the percentage error and the Root Mean Squared Error (RMSE) for each case using the following equations:

$$\%err = \text{mean}\left(\frac{\|k_i - k_{i\text{-}sim}\|}{k_{i\text{-}sim}}\right), \tag{13}$$

$$RMSE = \sqrt{\frac{1}{n}\sum_{i=1}^{n}(k_i - k_{i\text{-}sim})^2}, \tag{14}$$

where, k_i is the stiffness value computed analytically at the ith angle α, and $k_{i\text{-}sim}$ is the corresponding value obtained from the FEM simulation. The variable n indicates the number of simulated angles.

3.4. Optimization of the dual-joint compliant mechanism

The method for optimizing the dual-joint compliant mechanism considering stiffness isotropy was based on a parametric analysis. This was performed varying the angle γ between the joints from 0° to 360° in 15° step. For each angular configuration, the RMSE was computed in relation to an ideal circular stiffness distribution, where the radius represents the mean stiffness value. The configuration with the smallest RMSE was then selected as the optimal option, as it provides the closed stiffness distribution to that of an ideal isotropic stiffness field.

For each loading direction α, the hybrid Analytical/FEM simulation returns the displacement of point C in Cartesian coordinates (dx_{tot}, dy_{tot} and dz_{tot}). We first compute the actual displacement direction, δ, in the $x-z$ plane

$$\delta(\alpha) = \text{atan2}\big(dz_{tot}(\alpha), dx_{tot}(\alpha)\big), \tag{15}$$

where δ is expressed in degrees and measured with respect to global x-axis. The angular mismatch between the direction of the applied load and the resulting displacement is then quantified by

$$\epsilon_{ang}(\alpha) = |\alpha - \delta(\alpha)|, \tag{16}$$

which provides a measure of the coupling with non-working directions within the $x-z$ plane.

Further analysis for informing the decision on the optimized dual-joint configuration focused on the parasitic displacement error of the RCM point (i.e., point O). This analysis was carried out numerically using FEM simulations in Ansys, estimating the displacement of O when the instrument shaft was subjected to a rotation of 4.5° from its central neutral position.

In addition to the in-plane stiffness in the x-z working plane, we also evaluated by a FEM analysis in ANSYS, the axial stiffness of the optimized dual-joint configuration. For this test, the same load used during the Hybrid Analytical/FEM simulation was applied at point C along the direction of the instrument shaft (vector connecting O to C), while point A was maintained fixed. The corresponding displacement of point C along $\overrightarrow{CO}$ was used to compute the axial stiffness.

3.5. Experimental validation

In the final phase of the study, we carried out an experimental validation of the dual-joint configuration that had emerged as the most promising in the previous analyses. The prototype was additively manufactured by selective laser sintering (SLS) in polyamide-12 (PA12), which is the same material used during the simulations described on Section 3.2. This process enables the production of complex geometries while providing suitable mechanical properties for structural testing.

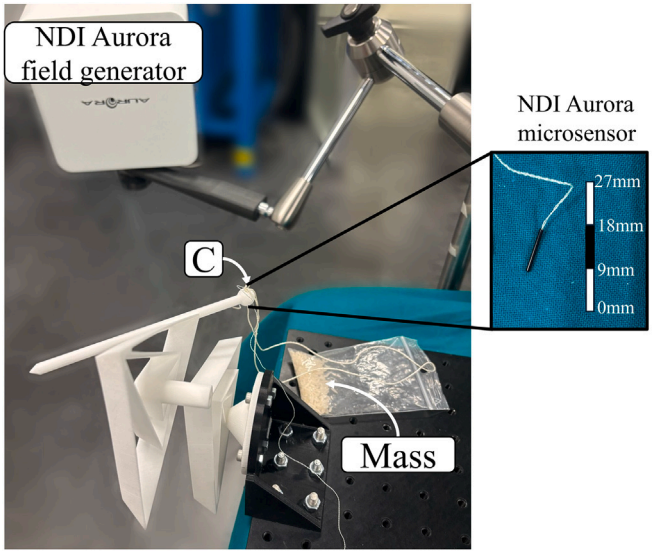

Fig. 6. Experiment setup used for finding the stiffness behavior on the dual-joint configuration.

Previous work has shown a close correspondence between FEM predictions and laboratory measurements for PA12, with stiffness deviations below 4% [20]. The dual-joint is produced by SLS with a 0° build orientation, corresponding to the configuration for which fatigue S–N curves have been reported in the literature [21]. Specifically the relation between the stress amplitude (S) and the number of cycle to failure (N) is

$$S = 111.1N^{-0.11}. \tag{17}$$

To characterize the mechanical response of the joint, an NDI 5DOF Aurora sensor was rigidly mounted at the prototype of the joint (Fig. 6). A blind hole was made at the point C, and the Aurora sensor was fully inserted so that the sensor tip coincided with the nominal position of point C. The dual joint mechanism was positioned within the measurement volume of the Aurora field generator, ensuring that the sensor remained inside the electromagnetic field. The Aurora system was operated with its default settings, providing position and orientation measurements at a rate of 40 Hz for each loading position direction, depending on the application angle α. The position of point C was acquired immediately before applying a force of 0.1 ± 0.01 N and again 20 s after the load application, allowing the joint to reach static equilibrium and letting vibrations decay. The displacement of point C was computed as the difference between the final and initial positions. The declared accuracy of this tracking system, reported as 95% Confidence Interval (95% CI) is 1.40 mm for positional accuracy and 0.35° for orientation accuracy. Here, 95% CI indicates that, under the manufacturer's specified test conditions, 95% of the measured errors are expected to fall within the stated bound. This accuracy allowed measuring of displacements of point C, producing a robust experimental basis for validating the stiffness behavior of the joint. Since the error on the RCM must be less than 1 mm, and the accuracy specified by the manufacturer does not satisfy this requirement, the Aurora sensors were not used to measure the parasitic displacement errors of the RCM.

The application angle α was varied by rotating the joint around the fixation point A rather than changing the direction of the load. Point A is realized as a modular fixation interface (visible in Fig. 8a) that allows the joint to be connected to the mounting plate in twelve discrete orientations, spaced by 30°. By reconnecting the joint at A in each of these orientations, the local direction of point C is rotated with respect to the global frame, while the loading device applies the same 0.1 ± 0.01

N force along a fixed direction. This results in twelve experimental configurations corresponding to $\alpha = 0°, 30°, 60°, \ldots, 360°$.

The force was set at 0.1 N for two reasons. First higher force values lead to collisions between the joint walls, leading to significant changes in stiffness. Second, the current prototype is manufactured in PA12, a relatively compliant plastic material. Such a material is appropriate for early prototyping, requiring comparatively small forces to produce measurable deflections. For each angular increment, ten displacement measurements were recorded, resulting in 120 total samples. The mean displacement was subsequently calculated for each direction. Finally, the displacement data collected were converted to stiffness values using Eq. (3).

3.6. Workspace determination

To guarantee safe deployment in the operating theater, the mechanism must allow the end effector to rotate by at least ±15° around the RCM, a range derived from anatomical dimensions of the third ventricle and pre-insertion alignment requirements.

The upper bound of the joint workspace was quantified experimentally. A force was gradually increased at point C of the prototype until mutual contact between opposing flexure walls caused a sharp increase in stiffness that prevented any further rotation. The displacements were then sampled by rotating the load direction about point C in 30° increments, mirroring the procedure described in Section 3.5 of the manuscript. Knowing that the end effector is 141 mm long, it is possible to obtain the rotation of the instrument using this relation.

$$\theta_{ee} = \arctan\left(\frac{\text{disp}}{\text{L}_{\text{ee}}}\right), \tag{18}$$

where θ_{ee} is the rotation of the end effector around the RCM, $disp$ corresponds to the displacement, and L_{ee} is the length of the end effector.

Five repeated measurements were taken for each of the twelve angular configurations, obtaining a total of 60 observations.

4. Results

4.1. FEM-based verification of the analytical dual-joint stiffness estimation method

To validate the strategy described in Section 3.1, which we used to estimate the stiffness of joints arranged in series, we performed a FEM analysis using Ansys software. We applied this validation to CAD models with angular configurations (γ) of 180°, 225°, 270° and 315°.

Fig. 7 shows the stiffness results of two distinct FEM-based strategies. A polar plot is used to capture the directional behavior of the joint over the full 360° range. The circular red markers represent stiffness values calculated by independently analyzing the two joint components and combining their displacements using rotation matrices, as described in Section 3.1. In contrast, the blue lines correspond to stiffness values derived from FEM simulations conducted directly on the complete CAD model of the selected sample.

Table 3 shows the percentage error and RMSE values computed between the stiffness values obtained analytically and from FEM simulation for each configuration. The maximum percentage error was 5.59% for 225° and the maximum value of RMSE was 0.42 N/m obtained in the configuration 315°. These results validate the proposed analytical approach for simulation studies of the dual-joint compliant mechanism.

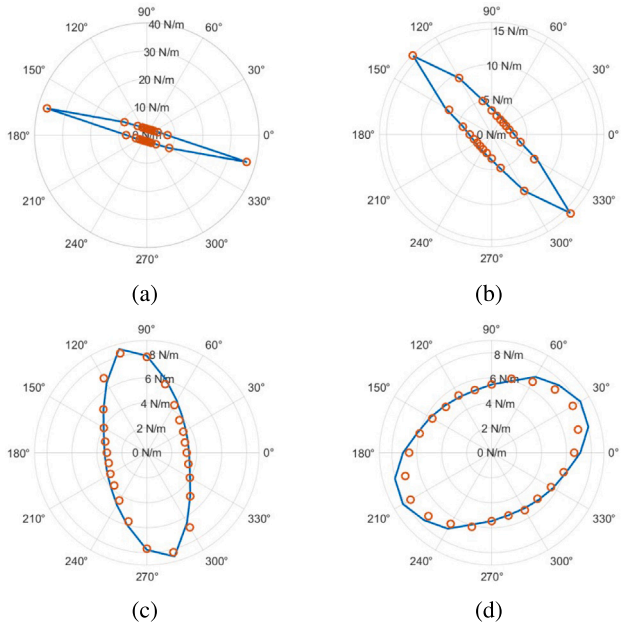

Fig. 7. Stiffness validation results obtained by hybrid analytical/FEM methodology (indicated by the red circle), compared with the FEM simulations conducted directly on the full dual-joint configuration (blue line) at (a) 180°, (b) 225°, (c) 270°, and (d) 315° angular offsets. (For interpretation of the references to color in this figure legend, the reader is referred to the web version of this article.)

Table 3
Percentage error and RMSE values computed between the stiffness values obtained analytically and from FEM simulation for different dual-joint configurations.

γ configuration	% Error	RMSE (N/m)
180°	3.29%	0.129
225°	5.59%	0.258
270°	5.06%	0.270
315°	4.78%	0.415

4.2. Mechanism optimization results

Data regarding the process of optimization of the dual-joint compliant mechanism are summarized in Table 5.

The results show that the configuration with an angle offset of $\gamma = 300°$ achieves the smallest RMSE of 0.90 N/m, and is therefore the closest to an ideal isotropic stiffness field. The polar stiffness profile of this configuration, reported in the FEM column of Table 4 and reproduced in Fig. 9b, varies from a maximum of 6.90 N/m at $\alpha = 60°$ and 240° to a minimum of 4.44 N/m at $\alpha = 150°$ and 330°.

For comparison, the single-joint reference configuration (Fig. 2) shows a much stronger directional dependence (Fig. 9a), with peak stiffness values of 314.81 N/m in $\alpha = 150°$ and 330°, and minima of 14.55 N/m in $\alpha = 60°$ and 240°.

In addition to the stiffness magnitude, we evaluated with the hybrid analytical/FEM simulation, how well the deformation direction follows the applied load. Table 6 reports, for each loading direction α, the displacement direction δ, after the force F was applied and the corresponding angular deviations $\varepsilon_{ang}(\alpha)$ between the load and displacement directions, computed as described in Section 3.4.

The results show that the configuration at $\gamma = 300°$ presents a maximum parasitic displacement of only 0.051 mm for a 4.5° rotation of the instrument shaft, corresponding to the intracranical operating range. This is a mere 4% of the parasitic displacement of the single-joint configuration, which results to be 1.10 mm. These results are

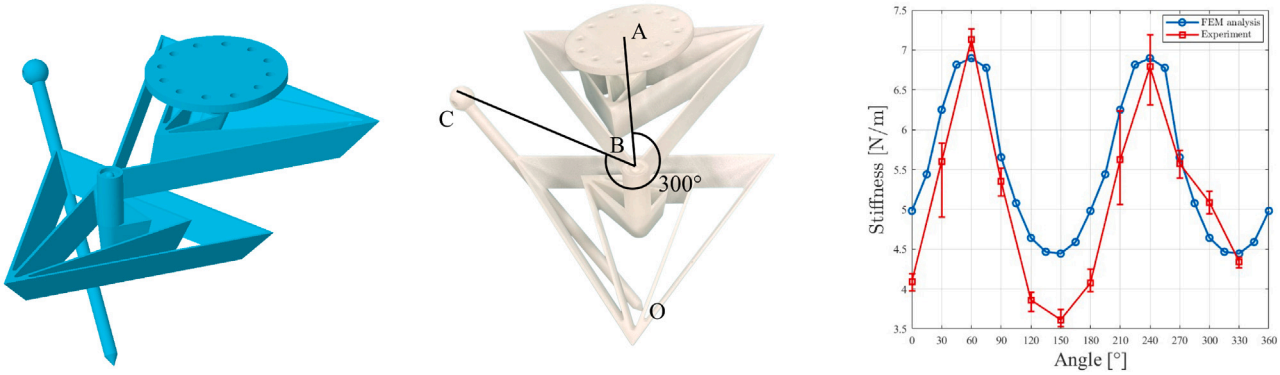

Fig. 8. (a) CAD model of the optimized dual-joint compliant joint mechanisms with $\gamma = 300°$. (b) Picture of the prototype realized in Nylon PA12. (c) Stiffness of the prototype obtained by FEM analysis (in blue) and experimentally (in red). (For interpretation of the references to color in this figure legend, the reader is referred to the web version of this article.)

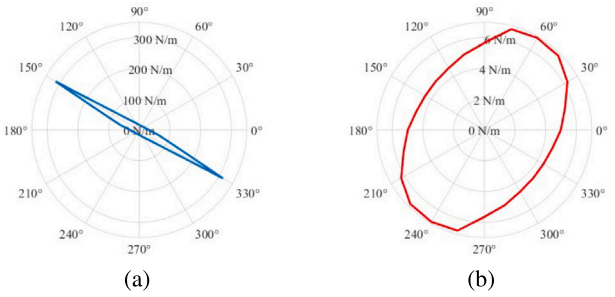

Fig. 9. Polar plots of directional stiffness for two different compliant mechanisms with RCM. (a) Single joint configuration. (b) Optimized dual-joint configuration. The azimuth α (0°–360°) indicates the applied force direction, while the radius expresses the corresponding stiffness.

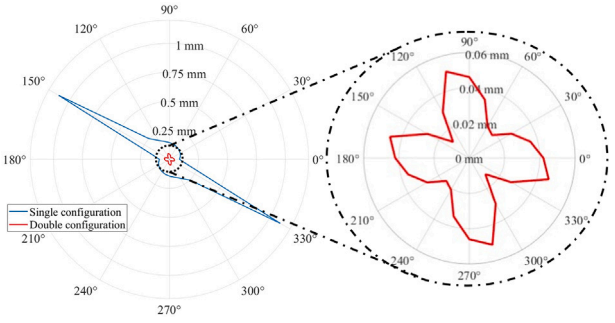

Fig. 10. Polar plot of parasitic displacement errors of the RCM of two different compliant joints estimated by FEM simulation for a 4.5° deflection of the instrument shaft in all possible directions. Results from a single joint mechanism are shown in blue, and those for the optimized dual-joint configuration are shown in red. The azimuth indicates the deflection direction, while the radius expresses the corresponding stiffness. (For interpretation of the references to color in this figure legend, the reader is referred to the web version of this article.)

summarized in Fig. 10. Besides the in-plane behavior, the axial stiffness of the optimized dual-joint was also assessed numerically.

Finally, for a load applied at point C along the shaft direction ($\overline{CO}$), the axial stiffness obtained was $k_{ax} = 173.34$ N/m.

Table 4
Comparison between experimental and simulated stiffness values across angular configurations. Each row reports the stiffness values obtained from both FEM simulations and experimental measurements for a given value of α. For each angular configuration, the maximum and minimum deviation, as well as the percentage error between FEM and experimental results, are provided.

α	Stiffness [N/m]				Error [%]
	FEM	Experiment	Deviations		
0°	4.98	4.09	0.10	−0.12	17.85
15°	5.44	–	–	–	–
30°	6.25	5.60	0.23	−0.69	10.39
45°	6.82	–	–	–	–
60°	6.90	7.14	0.13	−0.14	3.44
75°	6.78	–	–	–	–
90°	5.65	5.35	0.17	−0.18	5.43
105°	5.08	–	–	–	–
120°	4.64	3.86	0.10	−0.15	16.77
135°	4.47	–	–	–	–
150°	4.44	3.61	0.13	−0.09	18.69
165°	4.59	–	–	–	–
180°	4.98	4.08	0.17	−0.11	18.20
195°	5.44	–	–	–	–
210°	6.25	5.62	0.62	−0.56	10.08
225°	6.82	–	–	–	–
240°	6.90	6.79	0.40	−0.48	1.58
255°	6.78	–	–	–	–
270°	5.65	5.57	0.17	−0.18	1.45
285°	5.08	–	–	–	–
300°	4.64	5.09	0.14	−0.14	9.64
315°	4.47	–	–	–	–
330°	4.44	4.34	0.05	−0.08	2.26
345°	4.59	–	–	–	–

4.3. Experimental validation results

Experimental validation of optimized configuration was carried out using the Nylon PA12 prototype shown in Fig. 8(b), which was equipped with NDI Aurora electromagnetic sensors for high-accuracy displacement tracking. The results of the experiment performed are presented in Fig. 8(c) and Table 4, which include comparison with results obtained by the FEM analysis.

4.4. Workspace results

The maximum workspace of the dual-compliant joint was experimentally evaluated using the Nylon PA12 prototype. As in previous tests, NDI Aurora electromagnetic sensors were employed to measure the displacement of the instrument tip, which was then converted into

Table 5
RMSE values from the ideal circle for different angle configurations.

Angle Configuration	RMSE from ideal circle [N/m]
0°	9.41
15°	9.47
30°	10.12
45°	9.48
60°	8.04
75°	6.40
90°	5.70
105°	5.87
120°	7.38
135°	10.18
150°	7.37
165°	5.44
180°	9.16
195°	6.40
210°	3.87
225°	3.75
240°	2.92
255°	2.25
270°	1.70
285°	1.24
300°	**0.90**
315°	1.07
330°	2.16
345°	3.75

Table 6
Displacement components and angular deviation for the dual-joint compliant mechanism.

α [°]	dx_{tot} [mm]	dz_{tot} [mm]	δ [°]	ϵ [°]
0	52.605	22.955	−23.575	23.575
15	46.912	15.512	−18.297	33.297
30	38.591	2.253	−3.341	33.341
45	27.959	−11.448	22.267	22.733
60	15.112	−24.629	58.468	1.532
75	4.501	−31.920	81.973	6.973
90	−14.796	−43.693	108.708	18.708
105	−29.608	−46.873	122.280	17.280
120	−43.478	−45.790	133.517	13.517
135	−53.350	−40.176	143.018	8.018
150	−59.719	−31.465	152.216	2.216
165	−61.720	−20.669	161.486	3.514

Note - Values for 180–350° omitted for symmetry.

Table 7
Workspace of the dual-compliant joint under varying force directions α. Each row reports the average rotation angle of the end-effector, along with the corresponding maximum and minimum deviations.

α	Average (°)	Max deviation (°)	Min deviation (°)
0°	33.84	1.56	−1.10
30°	30.92	0.85	−1.12
60°	30.48	1.48	−0.89
90°	27.99	0.31	−0.55
120°	27.73	0.79	−1.06
150°	35.60	1.08	−1.05
180°	33.32	2.00	−3.07
210°	33.31	2.26	−2.07
240°	18.42	1.31	−0.76
270°	20.08	0.86	−1.14
300°	20.05	0.62	−1.03
330°	34.47	0.70	−0.44

angular rotation about the RCM. The resulting data are presented in Fig. 11 and summarized in Table 7.

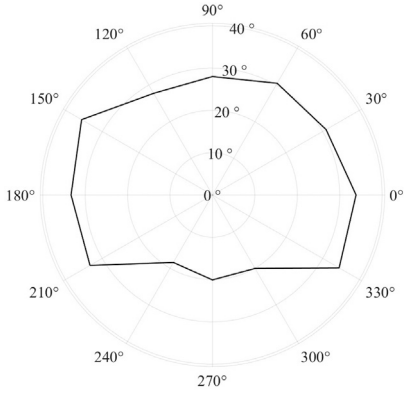

Fig. 11. Rotational workspace of the optimized dual-joint expressed in degrees around y-axis.

5. Discussion

The proposed monolithic compliant joint design stems from the idea of designing a new medical device to help surgeons perform Endoscopic Third Ventriculostomy (ETV). The objective is to address limitations commonly observed in rigid-link RCM systems, particularly the increased friction, backlash, and mechanical complexity introduced by multiple articulations. Using the elasticity of Nylon PA12, the structure avoids relying on ball bearings or sliding interfaces, reducing the risk of debris accumulation and potential malfunctions of the mechanism.

The proposed new joint advances previous work towards clinical implementation. Specifically, it improves the Tetra II joint design previously proposed by Rommers et al. [14], which can orient an instrument shaft around a remote center of motion constraint.

The first key design change consisted in relocating the instrument shaft from the central axis to an off-center position. This improves surgeon visibility of the surgical field and facilitates the use of a sterile drape for isolating components that cannot be sterilized for surgical use. It also facilitates the implementation of a quick disconnect solution that allows easy releasing the surgical instrument in case of failure or emergency. The resulting geometry still preserves the RCM functionality, minimizing tissue damage at the burr-hole insertion point.

A central motivation for this study was the observation of the suboptimal stiffness behavior of the single compliant joint and of its parasitic RCM displacement error when orienting the instrument shaft. This led to the proposal of a dual-joint compliant mechanism to achieve better performance while maintaining the RCM feature. Here, the behavior of this new joint was analyzed and optimized through simulations. An analytical model was developed, validated and used in the optimization process, providing gains in terms of simulation complexity and required CAD modeling efforts.

For better understanding of the improvements in the optimized joint, we compared its results with those from a single joint mechanism. The single joint configuration shows severe anisotropy, showing high levels of stiffness that can prevent orientation many different directions. The proposed dual-joint, on the other hand, can minimize stiffness anisotropy. The superiority of the dual-joint compliant mechanism was quantified based on three key metrics:

$$k_{\text{aniso}} = \frac{K_{\max}}{K_{\min}}, \tag{19}$$

$$\bar{K} = \frac{K_{\max} + K_{\min}}{2}, \tag{20}$$

$$\text{CV} = \frac{K_{\max} - K_{\min}}{\bar{K}}. \tag{21}$$

Table 8
Anisotropy and stiffness indicators for the two configurations.

Metric	Single joint	Dual joint
$K_{\max}$ [N/m]	314.81	6.90
$K_{\min}$ [N/m]	14.55	4.44
k_{aniso}	21.63	1.55
CV [%]	182.32	43.27
$\bar{K}$ [N/m]	164.68	5.67

In Eq. (19), k_{aniso} corresponds to the anisotropy factor. It drops from 21.6 to 1.55, which means that the most stiff direction is only ~ 1.5 times stiffer than the most compliant direction in the dual-joint mechanism, as opposed to more than 20 times in the single-joint one. In Eq. (20), $\bar{K}$ corresponds to the mean value of k, which decreases by almost two orders of magnitude (165 to 5.7 N/m) when upgrading the design to the two-joint configuration. Finally, the Coefficient of Variation (CV), defined in Eq. (21), is reduced by a factor of ≈ 4 (from 182% to 43%).

All results for the three metrics and also for the maximum (K_{max}) and minimum stiffness (K_{min}) values of the two joints designs are shown in Table 8. They show that the dual-joint configuration is nearly isotropic and demands far lower actuation torques, which will enable finer motion control and the use of low-power actuators to drive the mechanism.

The additional FEM analysis of axial loading confirms this behavior: while the dual-joint remains compliant and nearly isotropic in the x–z working plane, it exhibits a much higher stiffness along the shaft direction, showing an axial stiffness of 173.34 N/m. For comparison, the in-plane stiffness of the optimized dual-joint configuration ranges between 4.44 N/m and 6.90 N/m, indicating that the joint is roughly thirty times stiffer along the endoscope axis than in the intended pivoting directions. This provides robustness against inadvertent axial forces on the neuroendoscope without compromising the desired pivoting capability about the RCM.

The subsequent experimental phase focused on verifying stiffness uniformity under a 0.1 ± 0.01 N load. The measured stiffness data aligned with the FEM predictions, confirming that the dual-joint arrangement effectively mitigates stiffness spikes. Analyzing Table 4, it is evident that the most significant discrepancies between the experimental and simulated stiffness values occur at 150° and 180°, where the percentage errors reach 18.69% and 18.20%, respectively. These deviations suggest a local mismatch between the modeled joint and the real-world mechanical response in specific angular configurations, possibly due to nonlinearities, defects that may occur during the additive manufacturing process, or unmodeled deformations in those directions. In contrast, the smallest errors are observed in 270° and 240°, with percentage differences of only 1.45% and 1.58%, respectively. These low-error zones indicate strong agreement between simulation and experiment, suggesting that the stiffness behavior is more predictable and stable in these orientations. A similar trend is observed at 330°, with an error of just 2.26%.

In addition to the stiffness magnitude, we also evaluated the misalignment between the load direction and the resulting displacement in the working plane, quantified by the angular error ϵ_{ang}. For the dual-joint configuration, ϵ_{ang} remains below about 8° in the neighborhood of the loading angles $\alpha = 60°, 150°, 240°$ and 330°, indicating that the structure deforms almost collinearly with the applied load in these directions. Notably, these angles coincide with the directions where the stiffness analysis shows the maximum and minimum stiffness values. Conversely, for other loading directions ϵ_{ang} becomes much larger, with a maximum deviation of $\epsilon_{ang} = 33.30°$ for $\alpha = 15°$, revealing a stronger coupling with non-working directions and a less favorable alignment between load and deformation. These deviations arise from internal force coupling in serial flexure architectures. However, this effect is not expected to occur during the intended use of the joint in the surgical environment. In the final system, point C will be connected to two linear actuators (or two ball screws in a manual implementation) that drive the end-effector in the $x - z$ plane. In this displacement-controlled configuration, the motion of the end-effector is kinematically constrained to follow the actuator axes, so the commanded direction in the $x - z$ plane coincides with the actual motion direction, effectively suppressing the angular deviation ϵ_{ang}.

Although the primary objective of the experiments was the study of stiffness isotropy, parasitic displacements of the RCM point were also recorded to assess the performance of the mechanism. In the single-joint configuration, a rotation of the end effector of 4.5° resulted in a maximum parasitic error of 1.10 mm and an average error of 0.21 mm. In contrast, the dual-joint configuration reduced the maximum parasitic error to 0.051 mm and the average error to 0.032 mm. This corresponds to a 94.45% reduction in maximum displacement and a 84.29% reduction in average displacement compared to the single-joint configuration.

Even though the parasitic error at the RCM is lower in the dual-joint configuration, this does not imply higher stiffness than in the single-joint arrangement. In fact, the transition from a single joint to a dual joint reduces stiffness at point C.

Further analysis revealed that parasitic errors were generally more pronounced at angular positions associated with higher stiffness, and this was consistent between single- and dual-joint systems. However, in the dual-joint system, the error peaks of each joint occurred at different angles due to the 300° phase shift, resulting in a combined profile in which the peaks were angularly offset and effectively dampened. This angular desynchronization is key in minimizing net parasitic displacement, making the proposed architecture highly advantageous for surgical applications where submillimeter accuracy is essential.

The experimental evaluation demonstrates that the dual-compliant joint comfortably exceeds the clinical requirement of ±15° rotation about the RCM, achieving mean excursions between $\approx 18°$ and $\approx 36°$ in all loading directions. This isotropic angular range ensures full coverage of the third ventricle workspace and provides a generous safety margin for pre insertion alignment.

Assuming linear elastic behavior in the small deflection regime, the parasitic RCM translation scales approximately with the angular excursion. This allows estimating the parasitic displacement for the full ±15° range used in the stiffness analysis, which results in a maximum value of 0.17 mm.

Future research shall explore alternative materials for the construction of proposed compliant joint, such as Nitinol. The biocompatibility, flexibility, and shape memory of this material are potentially ideal for this application. In addition, it may improve joint fatigue behavior and reduce the risks of mechanical failure [22]. Recently, it has been demonstrated that Nitinol structures can be realized using additive manufacturing methods [23–25]. Therefore, it is now feasible to realize and investigate our intricate joint design using this promising super-elastic material.

Finally, future research may also look into alternative geometries to realize compliant joints with RCM for surgical applications. For example, the investigation of pentahedron or hexahedron architectures may yield valuable insights into stiffness behaviors and parasitic errors.

6. Conclusions

This work presented the application-driven design of a monolithic compliant joint intended for robotic neuroendoscopy applications. A key focus was to provide an RCM for intuitive orientation of the surgical instrument in minimally invasive brain interventions while also reducing friction, backlash, and mechanical complexity. This was achieved using tetrahedral structures as previously introduced by the Tetra II, which was redesigned and advanced towards a future clinical application. The new design supports and facilitates sterile draping, the implementation of a quick-connect holder for the surgical instrument,

and improves visibility of the surgical scene. Furthermore, the proposed dual-joint compliant mechanism provides near-isotropic stiffness in the working plane (x–z), while preserving a high stiffness along the non-working (shaft) direction, thus minimizing parasitic displacement errors of the RCM point, delivering sub-millimeter position stability for the intended neurosurgical application. These benefits introduced by the proposed joint are expected to greatly contribute to the creation of a robotic device for neurosurgery. First, isotropic stiffness indicates identical mechanical behavior in all directions, which can simplify motor control, leading to more robust and safer systems. Second, the high stiffness along the instrument axis represents an intrinsic safety feature of the joint, as it suppresses unintended instrument motions by the surgeon and thereby reduces the risk of additional patient injury. Lastly, the minimal parasitic error on the RCM position allows surgeons to maneuver the surgical instrument with minimal risk of tissue damage at the brain entry point. The obtained results underscore the potential of the dual-joint mechanism in meeting neuroendoscopic requirements. Combining streamlined geometry, minimal mechanical interfaces, and practical sterilization options offers a potentially more reliable, smaller, and safer alternative to rigid link RCM systems for neurosurgery. Future work in this direction includes the integration of a motorized actuation system, the integration of a neuroendoscope holder, and testing of the system in phantom-based experiments [26].

CRediT authorship contribution statement

Federico Mariano: Writing – original draft, Visualization, Software, Methodology, Investigation, Formal analysis, Conceptualization. **Elena De Momi:** Writing – review & editing, Supervision. **Giovanni Berselli:** Writing – review & editing, Supervision. **Jovana Jovanova:** Writing – review & editing, Supervision. **Leonardo S. Mattos:** Writing – review & editing, Supervision, Resources, Project administration, Methodology.

Declaration of competing interest

The authors declare that they have no known competing financial interests or personal relationships that could have appeared to influence the work reported in this paper.

Appendix A. Supplementary data

Supplementary material related to this article can be found online at https://doi.org/10.1016/j.precisioneng.2026.02.012.

References

[1] Tosi U, Guadix SW, Souweidane MM. Neuroendoscopy: The state of the art. World Neurosurg 2023;178:305–10.

[2] Cinalli G, Cappabianca P, De Falco R, Spennato P, Cianciulli E, Cavallo LM, Esposito F, Ruggiero C, Maggi G, De Divitiis E. Current state and future development of intracranial neuroendoscopic surgery. Expert Rev Med Devices 2005;2(3):351–73.

[3] Al-Aish ST, Abdul Hussein AF, Al Sakini AS, Rifai M, Alshareefi ML, Al Azzawi MAD, Sarhan K, Alkousheh H, Belabaci Z, Jader A, et al. Comparative assessment of endoscopic and microsurgery resection for intracranial ventricular tumors: a meta-analysis of 3059 patients. Acta Neurol Belg 2025;1–27.

[4] Aksungur S. Remote center of motion (RCM) mechanisms for surgical operations. Int J Appl Math Electron Comput 2015;3(2):119–26.

[5] Zhang W, Wang Z, Ma K, Liu F, Cheng P, Ding X. State of the art in movement around a remote point: a review of remote center of motion in robotics. Front Mech Eng 2024;19(2):14.

[6] Hoshide R, Calayag M, Meltzer H, Levy ML, Gonda D. Robot-assisted endoscopic third ventriculostomy: institutional experience in 9 patients. J Neurosurg: Pediatr 2017;20(2):125–33.

[7] Varma T, Eldridge P. Use of the NeuroMate stereotactic robot in a frameless mode for functional neurosurgery. Int J Med Robot Comput Assist Surg 2006;2(2):107–13.

[8] Singh A, et al. Sensitivity analysis of a double-parallelogram based RCM mechanism used for MIS robots. Proc Inst Mech Eng Part C: J Mech Eng Sci 2023;237(20):4813–27.

[9] Laribi MA, et al. A design of slave surgical robot based on motion capture. In: 2012 IEEE international conference on robotics and biomimetics. IEEE; 2012, p. 600–5.

[10] Marinho MM, et al. A programmable remote center-of-motion controller for minimally invasive surgery using the dual quaternion framework. In: 5th IEEE RAS/EMBS international conference on biomedical robotics and biomechatronics. IEEE; 2014, p. 339–44.

[11] Chandrasekaran K, Somayaji A, Thondiyath A. Realization of a statically balanced compliant planar remote center of motion mechanism for robotic surgery. In: Frontiers in biomedical devices, vol. 40789, American Society of Mechanical Engineers; 2018, V001T07A011.

[12] Gaafar M, Elgammal AT, El-Betar A, Magdy M. Development of a flexure based mechanism for robotic micro-surgical applications. J Robot Control (JRC) 2025;6(3):1375–84.

[13] Farhadi Machekposhti D, Tolou N, Herder J. A review on compliant joints and rigid-body constant velocity universal joints toward the design of compliant homokinetic couplings. J Mech Des 2015;137(3):032301.

[14] Rommers J, et al. A new type of spherical flexure joint based on tetrahedron elements. Precis Eng 2021;71. http://dx.doi.org/10.1016/j.precisioneng.2021.03.002.

[15] Naves M, Brouwer DM, Aarts RG. Building block-based spatial topology synthesis method for large-stroke flexure hinges. J Mech Robot 2017;9(4):041006.

[16] Wiersma D, Boer S, Aarts RG, Brouwer DM. Design and performance optimization of large stroke spatial flexures. J Comput Nonlinear Dyn 2014;9(1):011016.

[17] Pluimers P, et al. A compliant On/Off connection mechanism for preloading statically balanced compliant mechanisms. Proc ASME Des Eng Tech Conf 2012;4. http://dx.doi.org/10.1115/DETC2012-71509.

[18] Duffner F, et al. Anatomy of the cerebral ventricular system for endoscopic neurosurgery: a magnetic resonance study. Acta Neurochir 2003;145:359–68.

[19] Wilson JT, Tsao T-C, Hubschman J-P, Schwartz S. Evaluating remote centers of motion for minimally invasive surgical robots by computer vision. In: 2010 IEEE/aSME international conference on advanced intelligent mechatronics. IEEE; 2010, p. 1413–8.

[20] Rybansky D, Marsalek P, Sotola M, Hroncek J, Drahorad L, Kusnir O, Prokop J. Design and behavior of lightweight flexible structure with spatial pattern reducing contact surface fraction. Polymers 2023;15(19):3896.

[21] Salazar A, Cano AJ, Rodríguez J. Mechanical and fatigue behaviour of polyamide 12 processed via injection moulding and selective laser sintering. Analysis based on Kitagawa-Takahashi diagrams. Eng Fract Mech 2022;275:108825.

[22] Wadood A. Brief overview on nitinol as biomaterial. Adv Mater Sci Eng 2016;2016(1):4173138.

[23] Yan Z, Zhu J-N, Borisov E, Riemslag T, Scott SP, Hermans M, Jovanova J, Popovich V. Superelastic response and damping behavior of additively manufactured nitinol architectured materials. Addit Manuf 2023;68:103505.

[24] Yan Z, Zhu J-N, Hartl D, Riemslag T, Scott SP, Petrov R, Hermans M, Jovanova J, Popovich V. Correlation between microstructural inhomogeneity and architectural design in additively manufactured NiTi shape memory alloys. Virtual Phys Prototyp 2024;19(1):e2396065.

[25] Lantada AD, Aguilar C, Martínez RZ, Rendón ME, Li M, Contreras-Almengor Ó, Ordoño J, Solórzano-Requejo W, Vasic M, Munoz-Guijosa JM, et al. Additive manufacturing of nitinol for smart personalized medical devices: Current capabilities and challenges. In: Biostec (1). 2024, p. 123–34.

[26] Mariano F, Abello C, Kamal N, Berselli G, De Momi E, Piatelli G, Mattos LS. Design and fabrication of a phantom head for robotic neurosurgery simulation. In: European robotics forum. Springer; 2024, p. 43–7.